

Chapter 2

A Comparison Between the Behavior of Nanorod Array and Planar Cd(Se, Te) Photoelectrodes¹

2.1 Introduction

The II-VI semiconductors CdSe and CdTe are appropriate materials for testing the merits of the nanowire-based solar cell design. These II-VI compounds are both direct gap, highly absorbing materials having band gaps (1.7 eV for CdSe and 1.4 eV for CdTe) well-matched to the solar spectrum. Both materials can be deposited by a number of techniques.⁶³⁻⁶⁵ Electrodeposition of CdTe and CdSe is well established,⁶⁶⁻⁷³ and the photovoltaic or photoelectrochemical cell performance of the electrodeposited forms of these materials is usually limited by low minority-carrier diffusion lengths in the absorber material.^{63, 74}

¹ Reproduced with permission from Spurgeon, J. M., Atwater, H. A. and Lewis, N. S., *J. Phys.*

Chem. C **112**, 15, 6186-6193 (2008). Copyright 2008 American Chemical Society.

When a deposition technique that does not induce one-dimensional growth is used, production of a nanorod array requires the use of a template.³⁵ Anodic aluminum oxide (AAO) templates have been demonstrated to facilitate the electrodeposition of arrays of II-VI semiconductor nanorods.^{73, 75, 76} The pores in AAO templates are dense, relatively uniform in dimension, and highly vertically aligned (Figure 2.1). These pores can be fabricated with controllable pore aspect ratios, with pore diameters ranging from 5 nm to 200 nm, and with densities as high as 10^{11} pores cm^{-2} .^{44, 77} AAO templates can be formed by anodization of Al under a bias of 10 – 100 V in an acidic solution of sulfuric acid, phosphoric acid, or oxalic acid,⁷⁸⁻⁸¹ or are commercially available. AAO membranes are particularly compatible with electrodeposition methods because the insulating nature of the alumina prevents material from depositing directly onto the template. After fabrication of the rods, the template can be selectively removed in an aqueous solution of sodium hydroxide, leaving behind a freestanding, vertically aligned semiconductor nanorod array.

Validation of the theoretical, radial junction nanorod predictions³³ requires a direct comparison between the performances of planar and nanorod array geometries in systems in which high-quality, conformal, rectifying contacts are made for each type of microstructure. The use of a liquid junction is advantageous for such situations. The chemistry involved with obtaining stable photoelectrochemical cells using CdSe or CdTe has been well developed.⁸²⁻⁸⁷ Studies of the photoelectrochemistry of electrodeposited Cd(Se, Te) alloy layers are of particular relevance.⁸⁸ We describe herein photoelectrochemical studies of arrays of vertically aligned nanorods of Cd(Se, Te) in contact with rectifying, stable, liquid electrolytes, and compare the performance of such

electrodes to the behavior of photoelectrodes formed from analogous, planar Cd(Se, Te) materials. In addition, the spectral response of solid/liquid junctions with both planar and nanorod absorber microstructures has been obtained to elucidate the carrier collection properties as a function of the light absorption depth in the two different systems.

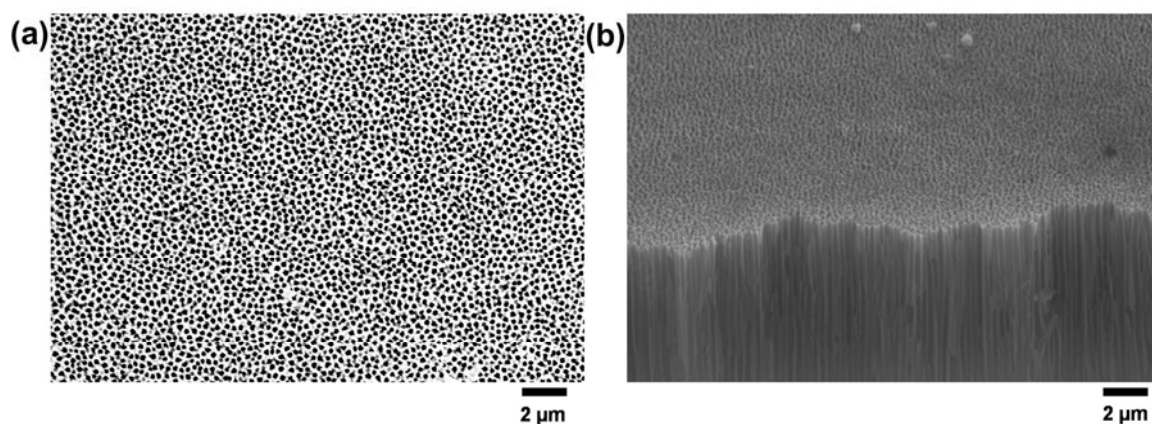


Figure 2.1. Anodic aluminum oxide (AAO) templates. (a) Top-down and (b) tilted cross-sectional view SEM images of 200 nm diameter pore AAO templates used to fabricate Cd(Se, Te) nanowire arrays.

2.2 Nanorod Array and Planar Electrodes

2.2.1 Electrode Fabrication

Nanorod array electrodes were fabricated using commercially available, 60 μm thick, 200 nm pore diameter, AAO membranes (Whatman Scientific) as templates. A 300 nm thick layer of CdSe was sputtered (RF magnetron sputterer, CdSe sputter target of 99.995% purity, Kurt J. Lesker Company) onto one side of the AAO to cover the bottoms of the pores. An ohmic back contact was then made by sputtering 1.5 μm of Ti (99.995% purity Ti sputter target, Kurt J. Lesker Company) onto the back of the CdSe layer. The other

side of the AAO was then covered in a layer of mounting wax to prevent deposition of metal onto the bottoms of the pores in subsequent processing steps. The template was made into a working electrode by attaching a Cu wire and applying conductive Ag paint around the edge of the membrane. The wire was encased in a glass tube, and the wire contact area was sealed with epoxy.

To provide mechanical stability and support for the nanorod array after the removal of the template, $> 10 \mu\text{m}$ of Ni metal was electrodeposited onto the back of the Ti. The Ni substrate was galvanostatically electrodeposited at room temperature, under stirring, from an aqueous solution of 0.8 M nickel (II) sulfamate ($\text{Ni}(\text{SO}_3\text{NH}_2)_2$) and 0.6 M boric acid (H_3BO_3). In this process, a current density of 25 mA cm^{-2} was maintained for 1 hr between the working electrode and a Pt gauze counter electrode. The mounting wax was then thoroughly removed by several washes in acetone. $\text{CdSe}_{0.65}\text{Te}_{0.35}$ was electrodeposited into the pores using an aqueous deposition bath that contained 0.2 M CdSO_4 , 20 mM SeO_2 , and 10 mM TeO_2 in 1 M H_2SO_4 . Triton X-100 was also added (0.25%) to reduce the surface tension and to improve the quality of the deposit. In addition to the Pt gauze counter, a saturated calomel electrode (SCE) reference was used with the AAO working electrode. The electrodeposition was performed potentiostatically at -650 mV versus SCE, at room temperature, without stirring, for 5 to 30 min.

After growth of the nanorods, the AAO template was removed by submersion of the electrode assembly for 20 min into 1 M $\text{NaOH}(\text{aq})$. The nanorod array was then thoroughly rinsed in $18 \text{ M}\Omega \text{ cm}$ resistivity H_2O , dried, and detached from the Cu wire. The array was then annealed for ~ 90 min at 600°C in an Ar atmosphere that contained a small percentage ($\sim 0.2\%$) of O_2 . The nanorod array was then cut into smaller samples

(0.1 – 0.3 cm²), and the samples were made into electrodes for use in photoelectrochemical cell measurements. Figure 2.2 provides a schematic summarizing the fabrication steps of the nanorod array photoelectrodes.

Planar Cd(Se, Te) electrodes were prepared in a nearly identical fashion. Ti foil (99.5% purity, 0.25 mm thickness) was cut into squares (0.2 – 0.4 cm²), flattened, mechanically polished, and then made into electrodes in the same way as was done for the AAO templates. The Cd(Se, Te) layer was then electrodeposited exactly as it was for the nanorod arrays. After ~ 15 min of electrodeposition, the semiconductor deposit began to clump on the Ti substrate and easily fell off. The best-performing planar electrodes were therefore obtained by electrodeposition of the film until just before this phenomenon started. The planar electrodes were then annealed under exactly the same conditions as those used to make the nanowire array electrodes.

The morphology and dimensions of the planar and nanorod array electrodes were investigated using a LEO 1550 VP field-emission scanning electron microscope (FE-SEM). The microscope was equipped with an Oxford INCA Energy 300 X-ray energy-dispersive spectrometer (EDS) system that was used to measure the elemental composition of the samples.

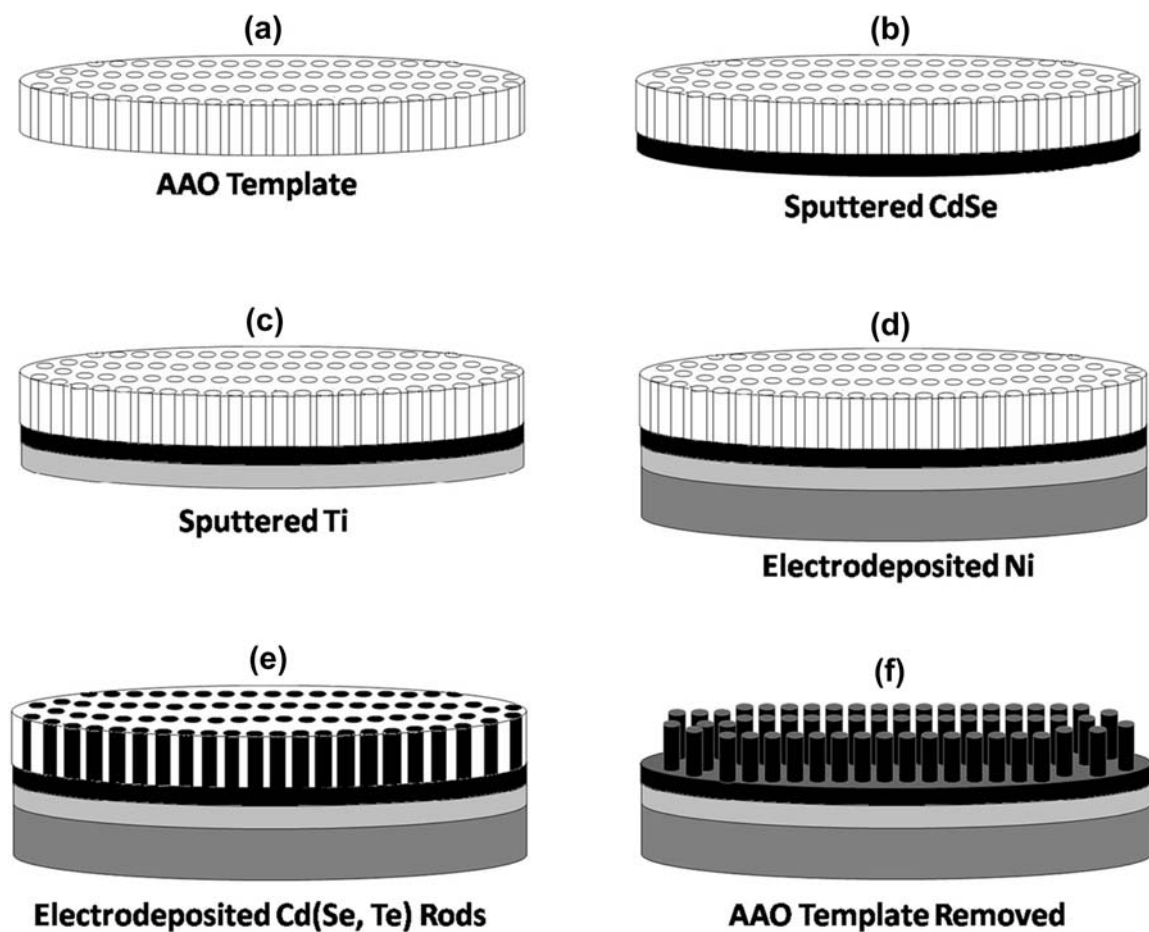


Figure 2.2. Schematic for the fabrication of nanorod array photoelectrodes. Starting with a commercially available (a) AAO template, a shunt-preventing layer was first applied by (b) sputtering a thin CdSe film on one side of the template, followed by (c) sputtering a Ti ohmic back contact layer. For structural stability, (d) Ni metal was electrodeposited on the back (note that to prevent growth of Ni inside the pores a wax layer was applied to the front of the template before electrodeposition and removed thoroughly with acetone afterwards). Nanorods were then grown by (e) electrodeposition of Cd(Se, Te) into the pores of the template (using wax on the back to prevent deposition in undesired areas). Finally, (f) the AAO template was removed with 1 M NaOH(aq), then rinsed, dried, annealed, and made into photoelectrodes.

2.2.2 Electrode Morphology and Composition

Figure 2.3 shows a cross-sectional SEM image of a Cd(Se, Te) nanorod array after the removal of the AAO template. The contrast in the substrate indicates the transition from the Ti ohmic back contact to the sputtered CdSe shunt-preventing layer. The Ni supporting layer is not visible in this image because the Ni separated from the Ti at the edges of the sample when the electrode was cut. EDS indicated that the elemental composition of the nanorods was Cd: Se: Te in the ratio 3: 2: 1, to within a few atomic percent.

Figure 2.4 displays top-view SEM images of planar and nanorod array electrodes. The planar sample exhibited an uneven morphology, as is typical of electrodeposited Cd(Se, Te) films that are not constrained within a template.⁸⁸ EDS results on the planar material indicated that the elemental composition was Cd: Se: Te in the ratio 3: 2: 1, to within a few atomic percent.

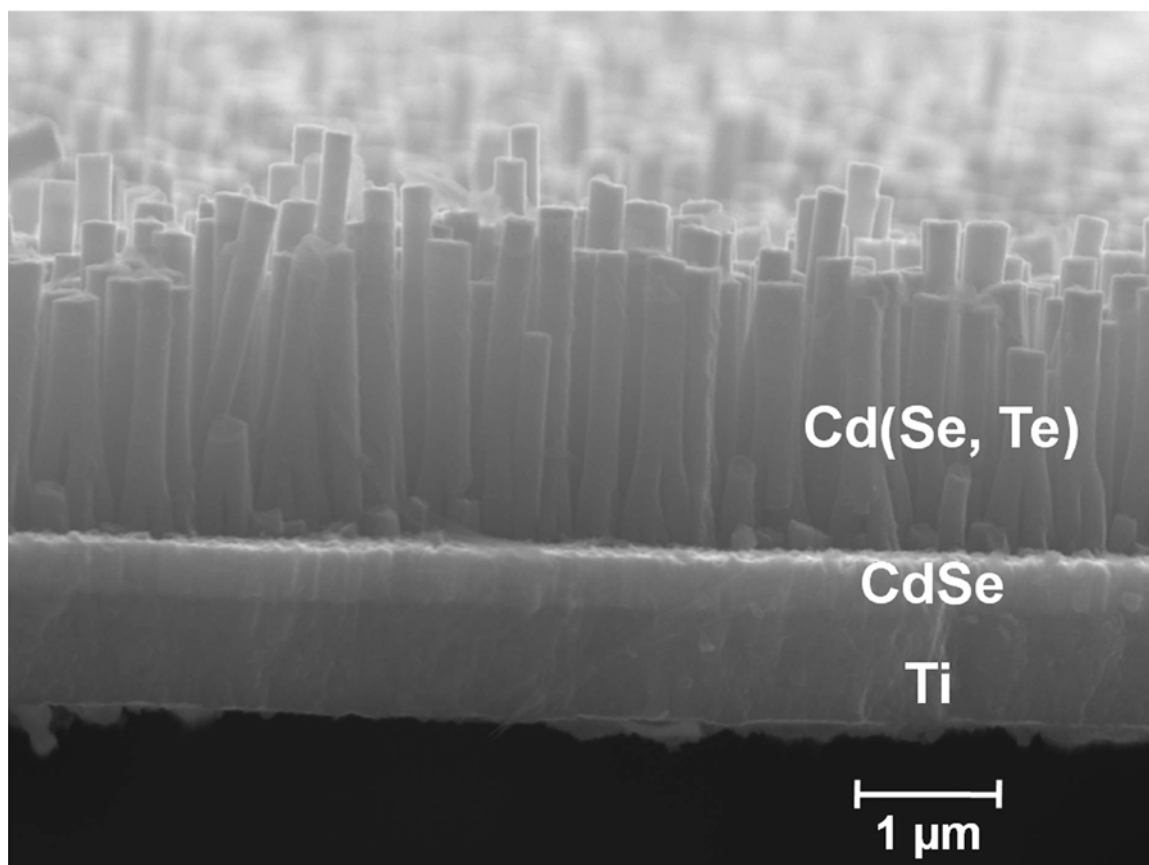


Figure 2.3. Nanorod array photoelectrode. SEM image (SE2 detector, 20 kV accelerating voltage) of a cross section of a Cd(Se, Te) nanorod array. The contrast in the substrate section indicates the shift from the Ti ohmic contact layer on the bottom to the sputtered CdSe shunt-preventing layer directly below the nanorods.

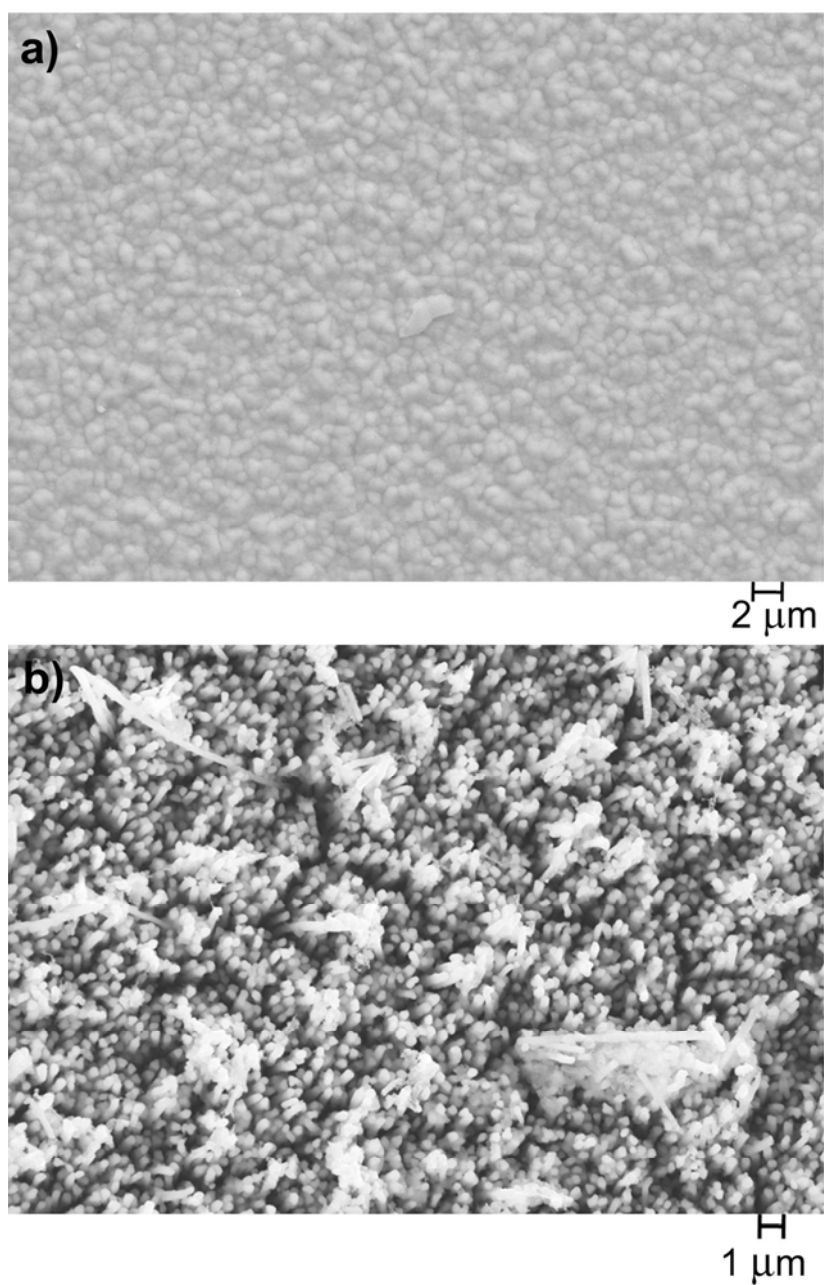


Figure 2.4. Planar vs. nanorod morphology. Top-down SEM images (SE2 detector, 20 kV accelerating voltage) of (a) a planar electrode showing the rough morphology characteristic of Cd(Se, Te) electrodeposition and (b) a nanorod array electrode displaying a typical, high density of nanorods ($> 10^9 \text{ cm}^{-2}$) with very uniform dimensions.

2.3 Photoelectrochemistry

2.3.1 Photoelectrochemical Cell Setup

The photoelectrochemical assembly consisted of the working electrode, a Pt gauze counter electrode, a Pt wire reference, and a liquid electrolyte, all in a glass cell. The electrolyte was 1 M Na₂S and 1 M S in aqueous 1 M NaOH, maintained under an Ar ambient. The cell potential determined at the Pt reference electrode was -0.76 V vs. SCE, which corresponds to the redox potential of the solution species and is in agreement with the literature value of the Nernst potential for this electrolyte.⁸⁹ The electrolyte was deoxygenated when made, and was kept under a positive pressure of Ar through the use of a Schlenk line. To prevent evaporation of the solution, the Ar was saturated with water vapor by bubbling the gas flow through 18 M Ω cm resistivity H₂O prior to introduction of the gas into the cell.

Current density vs. potential (*J-E*) data were measured using a Solartron SI 1287 potentiostat. Light from a Sylvania ELH-type halogen projector bulb was passed through a ground-glass diffuser to provide the equivalent of 100 mW cm⁻², as measured using a Si photodiode that had been calibrated relative to a secondary standard, NIST traceable, Si photocell calibrated at 100 mW cm⁻² of Air Mass (AM) 1.5 illumination. Before collection of *J-E* data, each electrode was allowed to reach equilibrium at open-circuit. *J-E* data were then measured on each electrode before and after a photoetch step. Photoetching was performed by immersing the electrode in a 90: 9.7: 0.3 H₂O: HCl: HNO₃ (v/v) solution for 10 s at short-circuit, under 100 mW cm⁻² of ELH-type illumination.

2.3.2 Current-Potential (*J-E*) Curves

Figure 2.5 displays the *J-E* behavior of a typical planar Cd(Se, Te) electrode under 100 mW cm⁻² of simulated AM 1.5 illumination. As expected for these electrodeposition conditions, the electrodes exhibited n-type behavior, passing cathodic current at forward bias and showing rectification towards anodic current flow in the dark.⁸⁸ For virtually every planar electrode tested, the photoetching step improved the short-circuit current density (J_{sc}), the open-circuit voltage (V_{oc}), and the fill factor, with the greatest improvement occurring in J_{sc} .⁹⁰ The annealing step was crucial for photoelectrode performance, as none of the unannealed samples, whether photoetched or not, displayed significant performance under illumination. Although an energy-conversion efficiency as high as ~ 4.1% was recorded for a planar Cd(Se, Te) electrode that had been photoetched and annealed, the majority of the photoetched and annealed planar Cd(Se, Te) electrodes exhibited energy-conversion efficiencies in the range of 1.5 – 3.0%. The thicknesses of the planar deposits were measured with SEM cross-sectional images to be between 2 – 3 μm.

Nanorod array electrodes were fabricated by electrodeposition of Cd(Se, Te) for times ranging from 5 min to 30 min. Those arrays that were measured to have the best performance under illumination had deposition times of 20 min, which corresponded to a total charge passed of 2 – 2.5 C cm⁻² of template area. SEM images revealed that the nanorods in these arrays varied in length from ~ 3.5 – 7.0 μm. In any particular array, however, the rods were within 1 μm of each other in length. These nanorod electrodes were also tested before and after the photoetching process.

Figure 2.6 shows the J - E behavior of one of the best-performing nanorod array electrodes. In many cases, the photoetching step significantly improved the efficiency of the nanorod array electrodes, as it did for planar electrodes. Photoetching of the nanorod arrays always increased J_{sc} , but only sometimes improved V_{oc} . For many of the nanorod electrodes, in fact, the photoetch step significantly reduced V_{oc} . Figure 2.7 displays the J - E behavior of one such cell.

Figure 2.8 and Table 2.1 present a direct comparison of the J - E behavior of planar versus nanorod electrodes. On the whole, the open-circuit voltage and short-circuit current density of the nanorod arrays were approximately half of the corresponding values for planar electrodes. The fill factors, on the other hand, improved relative to planar electrodes.

Control experiments were performed to evaluate the effect of the sputtered CdSe layer on the performance of the nanorod array electrodes. In these experiments, each step in the fabrication process of a nanorod array was followed, except for the deposition of Cd(Se, Te) into the pores of the template. The resulting electrode thus consisted of a thin layer of annealed CdSe on a Ti/Ni substrate. This electrode had a very low efficiency, of 0.11% before photoetching and 0.03% afterwards. Several planar electrodes were also fabricated with an identical sputtered layer of CdSe between the Ti back contact and the electrodeposited Cd(Se, Te) layer. The behavior of these planar electrodes was nominally indistinguishable from those that did not have the sputtered layer, with each such control electrode exhibiting values of the open-circuit voltage, short-circuit current density, and efficiency that were within the same distribution as those measured for samples that did not have the sputtered layer.

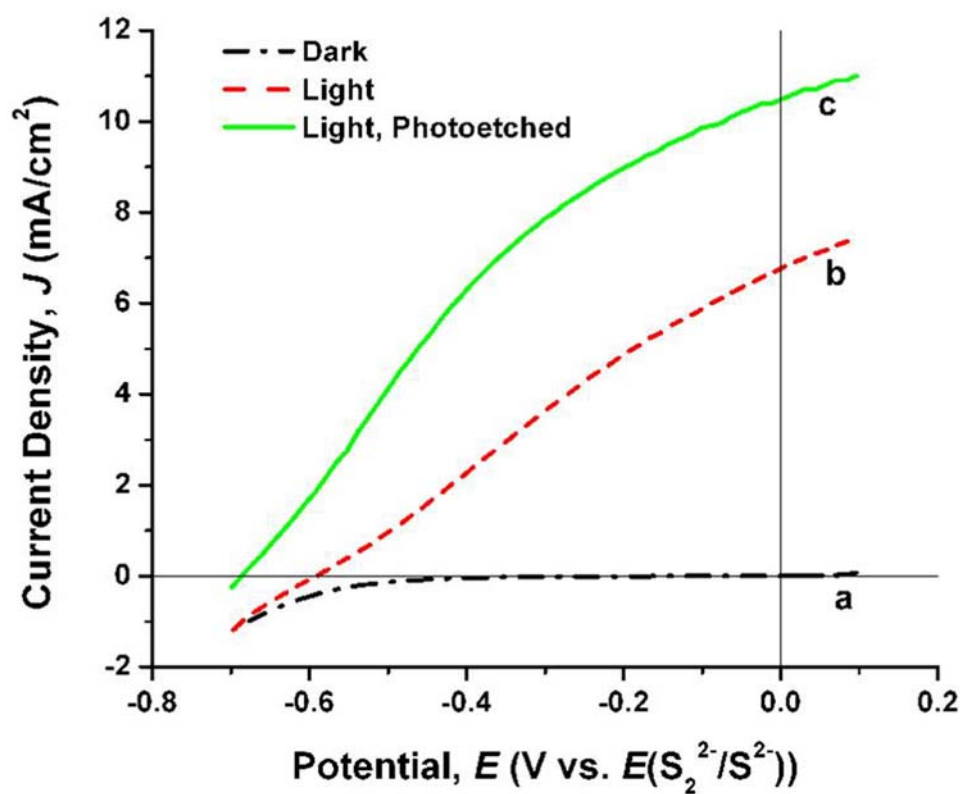


Figure 2.5. J - E data for a typical planar photoelectrode before and after photoetching. The black dashed-dotted line (a) is the behavior in the dark before photoetching (the behavior in the dark after photoetching was nominally identical, on this scale); the red dashed line (b) is the behavior in the light before photoetching; and the green solid line (c) is the behavior in the light after photoetching.

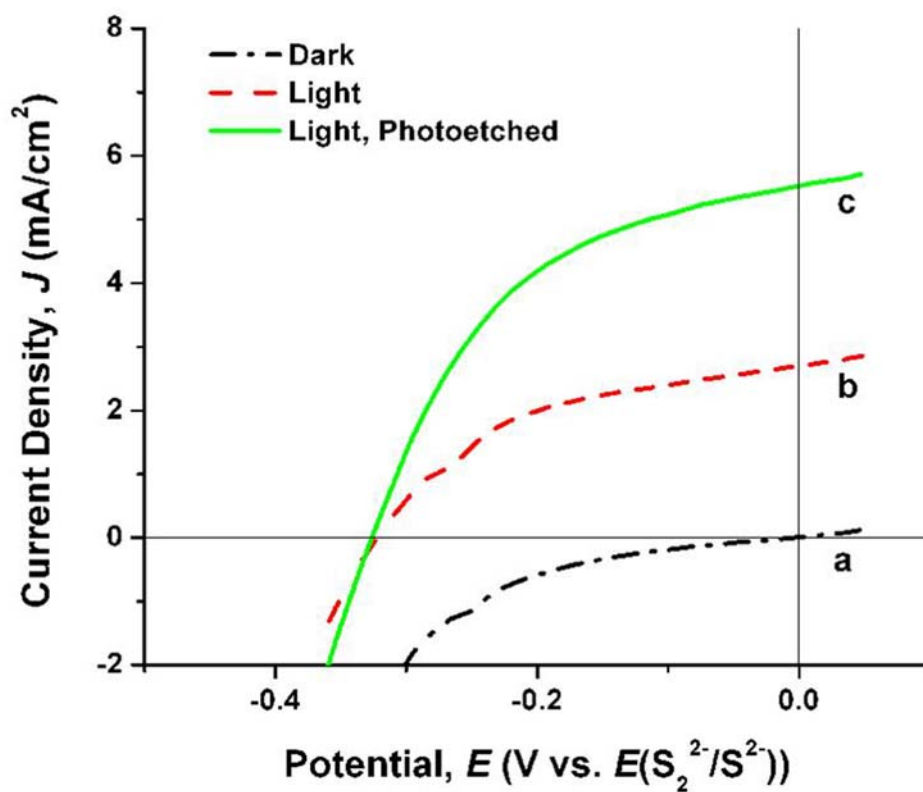


Figure 2.6. *J-E* curves of one of the best nanorod array electrodes before and after photoetching. The black dashed-dotted line (a) is the behavior in the dark before, or after, photoetching (no significant difference was observed between the two traces on this scale); the red dashed line (b) is the behavior in the light before photoetching; and the green solid line (c) is the behavior in the light after photoetching.

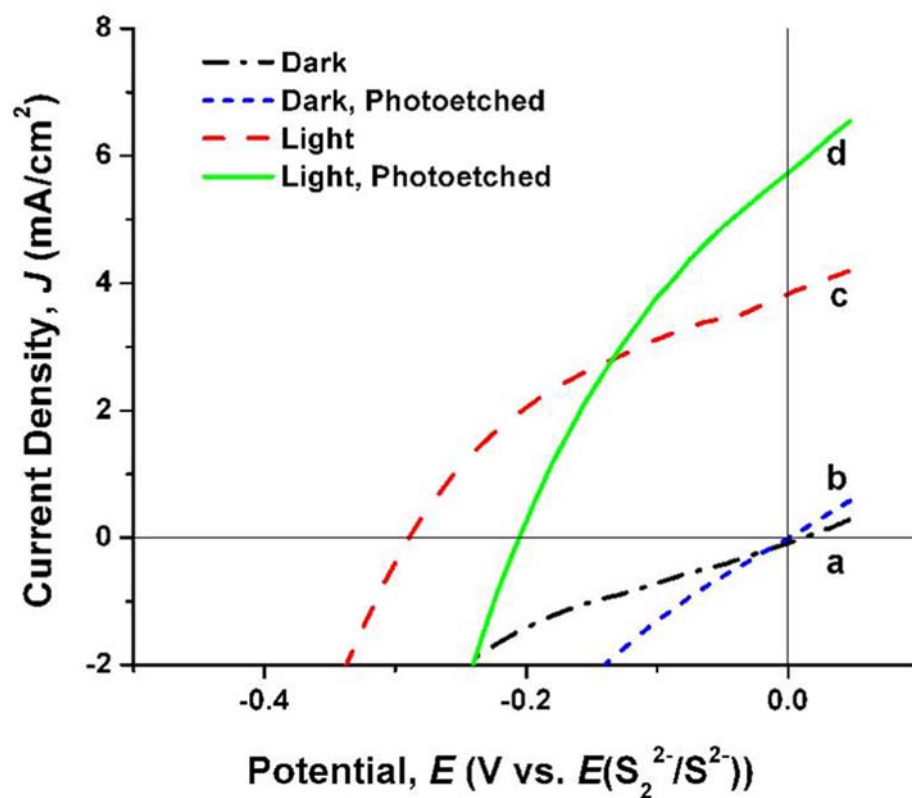


Figure 2.7. J - E data for a nanorod array electrode before and after photoetching. In this more common case, V_{oc} was reduced by the photoetch step. The black dashed-dotted line (a) is the behavior in the dark before photoetching; the blue short-dashed line (b) is the behavior in the dark after photoetching; the red dashed line (c) is the behavior in the light before photoetching; and the green solid line (d) is the behavior in the light after photoetching.

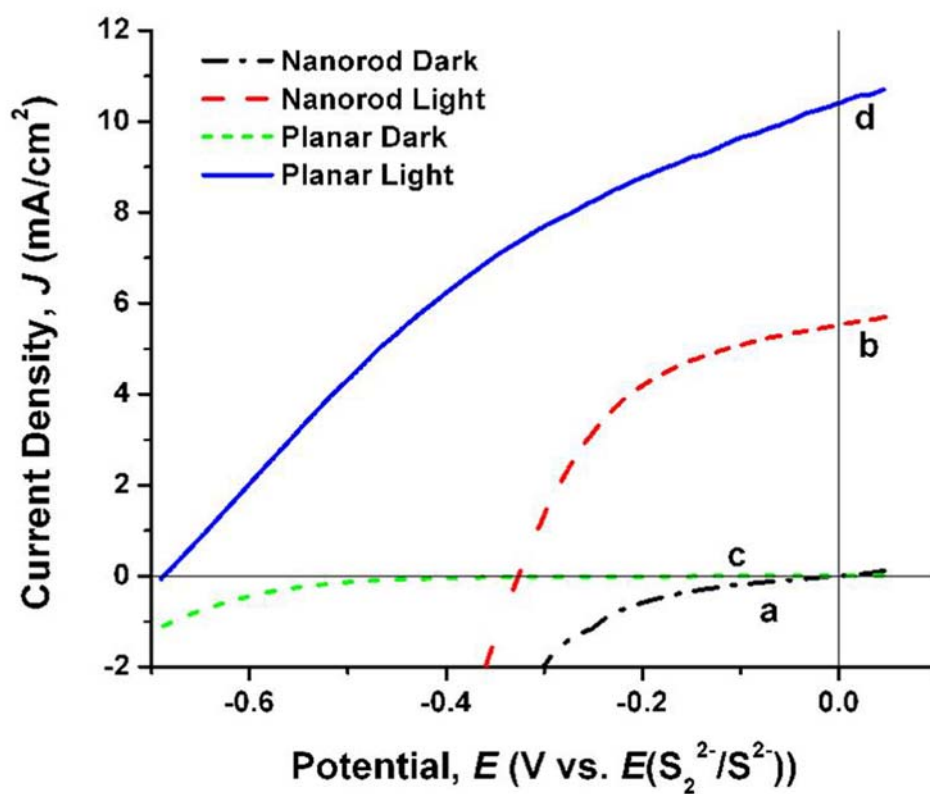


Figure 2.8. Comparison of the J - E curves of the planar and nanorod array cells. The responses shown are for photoetched electrodes. The black dashed-dotted line (**a**) is the behavior of the nanorod array in the dark; the red dashed line (**b**) is the behavior of the nanorod array in the light; the green short-dashed line (**c**) is the behavior of the planar electrode in the dark; and the blue solid line (**d**) is the behavior of the planar electrode in the light.

Table 2.1. Average J - E data for planar and nanorod array electrodes.^a

Electrode	V_{oc} (mV)	J_{sc} (mA/cm ²)	Fill Factor	Efficiency
Planar	557 ± 66	6.1 ± 0.8	0.288 ± 0.041	0.98 ± 0.16%
Photoetched Planar	650 ± 63	10.0 ± 3.4	0.358 ± 0.025	2.35 ± 0.95%
Nanorod	274 ± 36	4.0 ± 1.2	0.428 ± 0.051	0.45 ± 0.10%
Photoetched Nanorod	260 ± 27	5.6 ± 1.2	0.433 ± 0.055	0.62 ± 0.19%

^a The data are from 10 typical planar photoelectrodes and 7 nanorod array photoelectrodes that did not exhibit substantial reductions in open-circuit voltage with photoetching.

2.4 Spectral Response

2.4.1 System Setup

Spectral response measurements were performed immediately after each set of J - E data was obtained. The spectral response apparatus consisted of a 50 W Xe arc lamp, a quarter-wave monochromator equipped with 2.5 mm slits, a glass slide to direct a percentage of the beam to a reference Si photodiode, and an optical mirror to direct the remaining light onto the working electrode in the photoelectrochemical cell. The short-circuit current through the cell, and through the reference diode, was recorded simultaneously using two Princeton Applied Research Model 173 potentiostats. The absorbance of the liquid electrolyte was measured at each wavelength, using a UV-vis spectrophotometer.

2.4.2 Nanorod Array vs. Planar Normalized External Quantum Yield

As expected from the magnitude of the J_{sc} values, the planar electrode displayed a significantly higher external quantum yield than did the nanorod array electrode. A good planar electrode exhibited a maximum quantum yield of ~ 0.45 at 580 nm. In contrast, the best of the nanorod array electrodes exhibited a quantum yield of 0.29 at the same wavelength. Absorbance spectra taken on the polysulfide liquid electrolyte confirmed that the solution was highly absorbing at wavelengths, λ , < 500 nm, accounting for the decline in external quantum yield of the Cd(Se, Te) photoelectrodes at short wavelengths.

Although the external quantum yield of the planar electrode decreased with increasing wavelength, that of the nanorod array electrode stayed relatively constant until the onset of the band gap. Figure 2.9 depicts the spectral response data from two electrodes that were characteristic of the response of typical electrodes of each type. The data in Figure 2.9 have each been normalized to their respective points of highest quantum yield, so that the shapes of the spectral response data can be readily compared. The nanorod array electrodes exhibited a smaller decline in quantum yield near the band gap energy than did the planar electrodes, indicating that nanorod array samples more effectively collected minority-carriers generated from photons having longer penetration depths than planar electrodes.

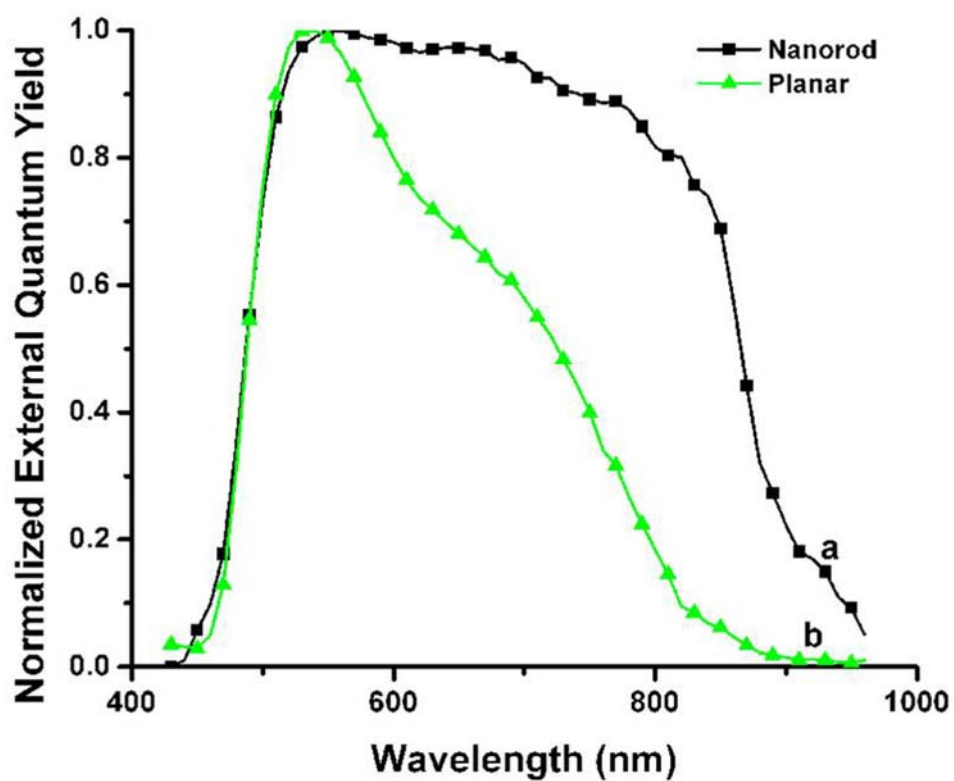


Figure 2.9. Spectral response of typical photoetched planar and nanorod array photoelectrochemical cells with the external quantum yield normalized to its highest value. The quantum yield of the nanorod array electrodes at wavelengths greater than 600 nm decreased less than that of the planar electrodes. The black solid line with squares (**a**) is the normalized spectral response of the nanorod array electrode, and the green solid line with triangles (**b**) is the normalized spectral response of the planar electrode.

2.5 Discussion of Nanorod Array vs. Planar Behavior

2.5.1 Spectral Response

The spectral response data indicate that the nanorod array electrodes behave as if they had a much longer minority-carrier collection length than planar electrodes made using nominally identical materials fabrication processes. In a planar electrode, photons of energies at or near the band gap energy penetrate deeply into the absorber, producing electron-hole pairs that are physically remote from the collecting junction. For absorbers having minority-carrier collection lengths shorter than the optical absorption depth, these remotely generated electron-hole pairs cannot be effectively collected at the junction, and such electrodes therefore suffer a loss in quantum yield at these excitation energies. CdSe, CdTe, and the Cd(Se, Te) alloys are direct band gap materials whose absorption coefficient rises relatively quickly as the photon energy is increased above the band gap energy. Hence, the monotonic increase in quantum yield for planar electrodes until very short wavelengths are approached (Figure 2.9) indicates that the minority-carrier collection length is relatively small in such samples, and the short-circuit photocurrent density and photoelectrode efficiency suffer from this materials-related deficiency.

The spectral response behavior of the nanorod electrodes affords a striking contrast to that of the planar electrodes. Photogenerated charge-carriers are effectively collected even for the deepest penetrating photons above the band gap energy. Hence, the nanorod array electrodes effectively combine long absorption depths with small minority-carrier collection lengths, offering a method for obtaining high short-circuit photocurrent densities even from low collection length materials.

Electrodeposited Cd(Se, Te) films have been reported to have a relatively low doping density. On films that were electrodeposited using nominally identical methods to those employed herein, the doping density has been estimated to be $\sim 10^{15} \text{ cm}^{-3}$, through use of the Gärtner model to analyze the response of photocurrent produced by monochromatic illumination as a function of the reverse bias voltage.^{88, 91} Such a doping level corresponds to a depletion width of $\sim 1 \text{ }\mu\text{m}$, implying that the nanorods in the arrays studied herein are essentially fully depleted of majority-carriers. Hence, for the nanorods under investigation, the collection length is dominated by the width of the space-charge region, with some relatively smaller contribution from diffusive minority-carrier transport. Regardless of whether diffusion or drift determine the minority-carrier collection length, the data are in accord with expectations that the nanorod geometry allows more efficient collection of photogenerated minority-carriers over a limited collection length than does a planar structure having a thickness sufficient to obtain full optical absorption throughout the solar spectrum.

2.5.2 Short-Circuit Photocurrent Density

The nanorod array electrodes did, however, exhibit lower overall short-circuit current densities than the planar electrodes, despite the improved relative quantum efficiency vs. wavelength for the nanorod array samples (Table 2.1). This likely reflects, at least in part, the lack of a complete filling fraction of the incident optical plane of the specific nanorod electrode arrays used in this work. The filling fraction (projected area of the rods divided by the total projected area of the rods and the voids in between) of the arrays was estimated to be only 0.3. Methods to prepare higher density nanorod arrays, with less

void area between the rods, are therefore of interest. Optical scattering should partly mitigate the lack of a high optical filling fraction of the nanorod arrays, and light trapping schemes can in principle be used to enhance the optical absorption in such systems. Although the planar samples were dark gray in color, the nanorod array electrodes were jet black. Hence, to some extent, light trapping is already occurring, but not with sufficient magnitude to produce the highest quantum yields that are possible from such systems.

2.5.3 Open-Circuit Voltage

A significant difference in performance between the nanorod array electrodes and the planar electrodes is in the open-circuit voltage, V_{oc} . The nanorod array electrodes clearly yielded smaller V_{oc} values than the planar electrodes (Table 2.1). The decline in V_{oc} for nanorods can in general be related to two factors, one inherent to the nanorod array geometry, and one that can in principle be manipulated with optimized materials processing and junction formation. The inherent effect is that the nanorod array electrodes distribute the photogenerated minority-carrier flux over a larger junction collection area than is present for a planar electrode geometry. Specifically, the ratio of the junction area for a nanorod array electrode to a planar electrode is:

$$\gamma = A_{NR}/A_P = (2\pi rh\rho_{NR}A_P)/A_P = 2\pi rh\rho_{NR} \quad (2.1)$$

where A_{NR} is the junction area of the nanorod array electrode, A_P is the area of the planar electrode junction, r is the radius of a single nanorod, h is the height of the nanorods, and ρ_{NR} is the density of nanorods (number of rods per unit of planar base area). Note that this definition of γ only considers the area of the sidewalls of the rods and neglects the

area of the top of the rods and of the base between rods. For the arrays used herein, $r \sim 100$ nm, $\rho_{NR} \sim 10^9$ nanorods cm^{-2} , and h varied from 3.5 to 7.0 μm . For a nearly optimum absorber thickness, i.e., with $h = n(1/\alpha)$, with $n \sim 2 - 3$ where α is the absorption coefficient, $\gamma \sim 19$ for the same radius and density rods. For the specific samples used herein, $\gamma \sim 22 - 44$. Hence, if the charge is collected over the entire nanorod surface and if the rate of production of photogenerated charge-carriers is the same for both samples, then the minority-carrier flux across the junction boundary will be less for each nanorod in the nanorod array electrode than is present across the same projected area for the planar junction system.

Because the open-circuit voltage is related to the photocurrent density across the junction area by the relationship:

$$V_{oc} = (nk_B T/q) \ln(J_{sc}/\gamma J_o) \quad (2.2)$$

where n is the diode quality factor, k_B is Boltzmann's constant, T is the temperature, q is the elementary charge, J_o is the reverse saturation current density over the actual junction area, and J_{sc} is the short-circuit photocurrent density per unit of projected device area, V_{oc} will be decreased in nanorod electrode arrays having $\gamma \gg 1$ relative to the value of V_{oc} produced by an analogous absorber and junction in a planar electrode arrangement. Note that for $\gamma \gg 1$ this inherent geometry effect will tend to bias the optimum design away from the smallest nanorod diameters, due to the resultant increased junction area of such systems. In the present case, the increased junction area per unit of projected area is a factor of ~ 30 , which will produce a decrease in V_{oc} of ~ 90 mV (higher for $n > 1$) for the nanorod array electrode relative to the planar electrode, if all other parameters are equivalent. Since the J_{sc} of the nanorod array electrodes was, however, lower than that of

the planar electrodes, an even lower V_{oc} will result from the theoretical limit of Equation 2.2 for such samples. Furthermore, Equation 2.2 does not account for the exponential light absorption along the length of the rod, which would yield reduced quasi-Fermi level separation relative to the material at the front surface of the cell and further reduce V_{oc} . This, however, is a second-order correction that would require a full analytical treatment to describe properly.

Surface and/or junction recombination, which is more important in systems having a higher junction area per unit of projected area than a planar system, can also lower V_{oc} in nanorod array electrodes. The value of V_{oc} for junctions between the Cd(Se, Te) electrodes and the S_2^{2-}/S^{2-} electrolyte is lower than the bulk recombination-diffusion limit, which is approximately 1.0 V under AM 1.5 100 $mW\ cm^{-2}$ conditions according to the Shockley diode equation.²⁹ This indicates that the limiting process at present is related to a recombination process associated with the solid/liquid junction. In addition, the full depletion of the nanorods under study will produce a lower value of the band bending in the nanorod arrays than in the planar samples. Hence, improved fabrication methods that increase the doping of the rods, and/or lower the J_0 of the solid/liquid contact are expected to produce an increase in V_{oc} for such systems, up to the value of the theoretical limit obtained from the Shockley diode equation using the junction-area-corrected relationship of Equation 2.2.

Experimental evidence that V_{oc} in these specific nanorod array systems is limited by junction-derived recombination is also provided by consideration of the effects of photoetching. The improvement in photoelectrode performance due to photoetching is believed to derive from the removal of surface recombination centers as well as a

reduction in the reflectivity of planar electrode samples by the photocorrosion of small pits in the surface.⁹⁰ The nanorod array electrodes appeared black and should inherently produce significant internal light scattering and light trapping. Nevertheless, photoetching improved the J_{sc} and external quantum yields of planar and nanorod array samples. In addition, photoetching improved the V_{oc} of some nanorod array electrodes but reduced the V_{oc} of the majority of the nanorod array electrodes. If photoetching occurs due to photocorrosion, and therefore produces a roughening of the surface,⁹⁰ surface recombination would then be increased due to the increased value of the junction surface area, thereby decreasing V_{oc} . In contrast, because charge-carriers have a propensity to remain in trap states, the photoetch step will selectively etch surface defects, thereby offering a mechanism to increase V_{oc} . The trade-off between these two competing effects could account for the observation that photoetching improved V_{oc} in some cases and lowered it in others.

2.5.4 Fill Factor

The nanorod arrays exhibited better fill factors than the planar samples investigated in this study. However, the fill factors measured here for the planar electrodes were low relative to values reported previously for electrodeposited Cd(Se, Te) in contact with the same liquid electrolyte.⁸⁸ Some cracking of the Cd(Se, Te) layer during the annealing step may have led to pinholes that could account for the lower fill factor. Nevertheless, using nominally identical electrodeposition conditions, the nanorod array electrodes consistently exhibited better fill factors than their planar counterparts. This difference is consistent with the well-documented slow interfacial hole-transfer kinetics of the S_2^{2-}/S^{2-}

electrolyte. These slow charge-transfer kinetics produce a competition for minority-carriers between collection across the interface and surface recombination, with the potential dependence of these processes determining the fill factor of the device.^{92, 93} Accordingly, use of electron-transfer catalysts and/or rapid, one-electron transfer donors as redox species has been shown to improve the fill factor of n-GaAs/KOH(aq)-Se₂²⁻-Se²⁻ junctions.⁹⁴ In such systems, increases in the surface area of the electrode can therefore tend to favor charge-transfer relative to surface recombination because, at constant light intensity, the minority-carrier flux to the junction is reduced as the internal junction area is increased. Such effects would lead to an improved fill factor for such systems, in accord with the observations reported herein.

2.5.5 Avoidance of Shunting

When a liquid junction contact is used in conjunction with a nanorod array electrode, a significant shunt conductance will be produced if the electrolyte directly contacts the back ohmic electrical contact. In this work, this issue was mitigated by sputtering a thin layer of CdSe over the bottoms of the pores of the AAO at the beginning of the electrode fabrication process. In this way, the Ti contact cannot be exposed to the liquid electrolyte. This procedure raises the question of whether the sputtered CdSe layer contributed significantly to the observed properties of the Cd(Se, Te) nanorod array photoelectrode. Control experiments were conducted using this sputtered layer alone, and the resulting performance was quite low in comparison to what was measured for nanorod arrays. Considering that only a fraction of this area could be exposed to light when the nanorods were present, the contribution of this sputtered CdSe layer to the overall performance is

therefore concluded to be minimal. Such methods therefore demonstrate that it is possible to grow nanorod array electrodes in a template, without the use of a single-crystal substrate of the material being grown to form the nanorod array, without significant shunting.

2.6 Conclusion

Nanorod arrays of Cd(Se, Te) were fabricated using porous alumina templates and their photovoltaic properties were compared with analogous, planar electrodes in a photoelectrochemical cell. Spectral response experiments on both types of electrodes showed that the nanorod arrays exhibited enhanced collection, relative to planar electrodes, of low energy photons absorbed far from the front surface of the cell. The ability of nanorod arrays to maintain relatively high quantum yields in the red is evidence that the theoretical expectation of this geometry to improve carrier collection in diffusion-limited systems is valid. Furthermore, nanorod arrays were observed to have improved fill factors relative to their planar counterparts, possibly attributable to an improved ratio of charge-transfer relative to surface recombination, as a result of increasing the internal junction area. However, open-circuit voltages for the nanorod arrays were less than half the values for planar electrodes. A combination of increased surface recombination and an inherent geometrical limitation contributed to this effect. While these results are encouraging for future nanorod solar cell designs, improvements in the fabrication of these electrodes will need to be made to take full advantage of the benefits offered by this geometry. In particular, lowering the junction recombination rate should lead to large

improvements in the nanorod solar cell. Using single-crystal rods in the array is one method by which this could be pursued. Deposition of the semiconductor with a higher doping density, so that full band bending can be achieved within each nanorod, could also lead to improvements in the performance of the cell.